ORIGINAL ARTICLE

Characterization of Cu²⁺ adsorption for eco-hydroxyapatite derived from limestone sludge via hydrothermal synthesis

Ya-Wen Lin[1] · Sheng-Yuan Peng[2] · Wei-Hao Lee[1] · Yan-Yu Lin[2] · Ming-Jui Hung[3] · Kae-Long Lin[2]

Abstract
This study developed a novel approach to the hydrothermal synthesis of eco-hydroxyapatite (eco-HPA) from recycled limestone sludge for the removal of Cu^{2+} from aqueous solutions. The resulting eco-HPA was characterized using X-ray fluorescence, thermal field emission scanning electron microscope, X-ray powder diffraction analysis, and Brunauer–Emmett–Teller surface area measurements. Under a hydrothermal temperature of 120 °C and Ca/P molar ratio of 1, this study obtained the nitrogen adsorption isotherm and desorption curves indicative of hydroxyapatite. Based on the IUPAC classification system, these are the type-IV adsorption isotherm curves of a mesoporous structure with an H3-type hysteresis loop. The same sample achieved an adsorption capacity of 210 mg/g. The adsorption kinetics closely fit the pseudo-second-order kinetic model ($R^2 = 0.9990$–1.000). Adsorption isotherms presented the strongest correlation with the Langmuir model ($R^2 = 0.97$–0.99), exceeding that of the Freundlich model ($R^2 = 0.91$–0.98). Taken together, these results demonstrate that the proposed eco-HAP is a viable low-cost environmentally friendly adsorbent with broad applicability for the removal of heavy metals from aqueous solutions.

Keywords Limestone sludge · Hydrothermal synthesis · Hydroxyapatite · Adsorption · Isothermal adsorption model

Introduction

Large quantities of limestone sludge are produced in the quarrying, cutting, and crushing of limestone. Limestone sludge, comprising 85% water and 15% limestone powder, poses a serious threat to the environment [1]. The United Kingdom produces roughly 21.2 million tons of limestone sludge per year, Greece produces 18 million tons, and Turkey produces 30 million tons [2]. Taiwan produces about 12,000 tons of limestone sludge every year, most of which is piled in areas adjacent to production facilities. When disturbed by heavy rains and wind, these materials pose a health hazard (e.g., asthma) [3]. Sludge is currently disposed of in sanitary landfills in Taiwan. However, rapid urbanization has made locating suitable landfill sites increasingly difficult. The increase in the demand for natural resources and a scarcity of environmentally acceptable solid waste disposal sites have motivated several municipalities in Taiwan to consider resource recovery as an alternative. The CaO that makes up roughly 60% of limestone sludge [4] can be reused as filling material, natural aggregate, asphalt mixture, cement replacement material, and light brick material [5].

Water pollution by heavy metals poses a significant threat to the environment worldwide. Unlike most organic pollutants, heavy metals can have direct or indirect adverse effects on plants and humans, even at very low concentrations. The nonbiodegradability and long-term persistence of heavy metals leads to their accumulation in organisms throughout the food chain with a range of corresponding health disorders [6, 7]. The use of copper (Cu) in the manufacture of pesticides, paper, electronics, automotive parts, and fertilizers has led to the continuous release of large quantities of copper(II) from industrial wastewater into the environment. Cu is an essential trace element for organisms in natural ecosystems; however, excessive Cu^{2+} is a serious problem [8, 9]. Numerous methods have been developed for

✉ Kae-Long Lin
kllin@niu.edu.tw

1   Institute of Mineral Resources Engineering, National Taipei University of Technology, Taipei City 106, Taiwan, R.O.C.

2   Department of Environmental Engineering, National Ilan University, Yilan City 260, Taiwan, R.O.C.

3   Department of Safety, Health and Environmental Engineering, Ming Chi University of Technology, New Taipei City 243, Taiwan, R.O.C.

the removal of heavy metals from water, including chemical precipitation, ion exchange, adsorption, membrane filtration, and electrochemical processing [10–14]. Adsorption methods tend to be simple, flexible, cost-effective, and easy to implement [15, 16]. Researchers have developed numerous adsorbents, including zeolites [17], montmorillonite [18], diatomaceous earth [19, 20], and hydroxyapatite [21]. Note that these adsorbents vary considerably in terms of removal efficiency, preparation complexity, and cost.

Hydroxyapatite (HAP; $Ca_{10}(PO_4)_6(OH)_2$) is a member of the apatite mineral family and the main component of bones and teeth in vertebrates. HAP is widely used in wastewater purification [22] and soil remediation [23], due to its ability to fix heavy metal ions, such as Zn^{2+} and Cu^{2+} [24]. The immobilization of metal ions on HAP surfaces involves a number of processes, including ion exchange, surface complexation, HAP dissolution to form new metal phosphates, and the replacement of Ca^{2+} in HAP with other metal ions during recrystallization [25–27]. Ayodele et al. [28] used hydroxyapatite from eggshells to remove copper and nickel ions from simulated industrial wastewater. Wang et al. [29] used hydroxyapatite-biochar nanocomposite for the adsorption of Pb(II), Cu(II) and Zn(II). Wang et al. [30] used microspheres of synthetic abalone shell to remove Cu^{2+} from an aqueous solution. Chen et al. [31] prepared hydroxyapatite from sewage sludge as an absorbent to remove Cu^{2+} and Cd^{2+} from aqueous solutions. This study examined the efficacy of using limestone sludge as a source of calcium in the hydrothermal synthesis of ecological HAP (eco-HAP) for the removal of Cu^{2+} from water. The resulting materials underwent characterization via X-ray diffraction (XRD), Brunauer–Emmett–Teller (BET) and thermal field emission scanning electron microscope (FE-SEM). This study also sought to identify key factors affecting the total Cu^{2+} adsorption, adsorption kinetics, and adsorption isotherms.

Materials and methods

Materials

The limestone sludge samples were collected from a stone processing plant rom Hualien County in Taiwan. Limestone sludge was washed with distilled water to remove impurities and dried in an oven at 105 °C overnight, whereupon the resulting solids were sieved to a particle size of 74 μm. The limestone sludge was alkaline (pH = 11.70), with a specific gravity of 2.91 and a density of 2.21 g/cm^3. The limestone sludge comprised the following: ash (86.31%), combustible matter (13.45%), and moisture (0.24%). The limestone sludge comprised the following: CaO (94.30%), MgO (1.97%), and SiO$_2$ (1.73%). Using X-ray powder diffraction (XRD), it determined that the main crystal phase limestone sludge was calcium carbonate (JCPDS No. 085-1108). PO_4^{3-} from (($NH_4)_2HPO_4$) (diamine hydrogen phosphate, 98.5%) with HNO_3 (nitric acid solution, 65%) was used to extract the Ca source. NaOH (sodium hydroxide solution, 65%) was used to adjust the alkalinity of the solution.

Hydrothermal synthesis of hydroxyapatite

The limestone sludge solids were dried and crushed to form a powder. This study dissolved 25 g of the powder in 100 mL of 3 M HNO_3 and then filtered the mixture. ($NH_4)_2HPO_4$ solution (100 mL) was gradually added to the resulting solution until Ca/P ratios of 1, 1.67, 2.33, and 3 were reached. NaOH solution was added to maintain the pH of the solution at 10. Mixture details are listed in Table 1. The resulting mixture was then sealed in a Teflon-coated stainless steel container to perform autoclave and hydrothermal conversion at 120–180 °C over a period of 8 h. The autoclave was allowed to cool naturally to room temperature, whereupon the resulting product was washed using deionized water, collected as a powder, and dried at 90 °C for 24 h prior to analysis.

Material characterization

The chemical composition of the raw materials was analyzed using an X-ray fluorescence analyzer (XRF, Rigaku NEX CG). The pore structure and crystallinity of the eco-HAP were determined by XRD (Rigaku Miniflex, Japan) using diffraction data collected between $2\theta = 5–80°$. In accordance with the methods outlined by Iqbal et al. [32], this study calculated % phase A as the sum of the area under the 10 main peaks centered at $2\theta = 10.28°, 22.88°, 25.84°, 28.98°, 31.72°, 32.62°, 40.05°, 45.27°, 45.27°$ and $45.24°$, as follows

Table 1 Sample codes and corresponding experimental conditions

Sample code	Ca concentration (mol/L)	(NH4)2HP04 (g)	Ca:P	Hydrothermal temperature (OC)
LA3	1.55	16.38	1.00	120 °C
LA5	1.55	9.83	1.67	120 °C
LA7	1.55	7.02	2.33	120 °C
LA9	1.55	5.46	3.00	120 °C
LB3	1.55	16.38	1.00	150 °C
LBS	1.55	9.83	1.67	150 °C
LB7	1.55	7.02	2.33	150 °C
LB9	1.55	5.46	3.00	150 °C
LC3	1.55	16.38	1.00	180 °C
LC5	1.55	9.83	1.67	180 °C
LC7	1.55	7.02	2.33	180 °C
LC9	1.55	5.46	3.00	180 °C

Eq. (1). The crystal size of eco-HAP was calculated using the Scherrer equation, as follow Eq. (2).

$$\%PhaseA = {Sum\ of\ area\ under\ XRD\ peak\ of\ phase\ A}/_{Total\ area} \times 100 \tag{1}$$

$$\Delta(2\theta) = {0.9\lambda}/_{Dcos\theta} \tag{2}$$

where $\Delta(2\theta)$ indicates the peak width at half maximum (002) reflection intensity; λ is the wavelength of CuKα (0.154056 nm); D (nm)) is the crystal size; and θ is the Bragg angle [33].

FE-SEM (Nova NanoSEM 230) was used to characterize the surface and structural morphologies. Nitrogen adsorption and desorption isotherms were obtained using a Tristar 3000 (Micromeritics) and the BET method was used to determine the specific surface area. The BJH method was used to calculate the total pore volume and pore diameter.

Batch adsorption

In a volumetric flask, $Cu(NO_3)_2$ was dissolved in deionized water to prepare a standard Cu^{2+} solution (100 mg/L). The solution was then diluted to the desired concentration using deionized water. The volume of the tested metals bearing aqueous solutions was fixed at 100 mL. All adsorption experiments were performed under a controlled temperature with the contents of the flask stirred at 100 rpm. This study examined the adsorption of Cu^{2+} by eco-HAP as a function of the following adsorption conditions: adsorbent quantity (0.1–2 g/L), reaction time (0–180 min), and initial Cu^{2+} concentration (10–100 mg/L) The pH of the solution was maintained at 5 through the addition of 0.1 M of NaOH solution. All experiments were performed in triplicate to confirm their reproducibility, the results of which were averaged. Note that the relative standard deviation was less than 3% of the average. Immediately after adsorption, the samples underwent solid–liquid separation using a centrifuge, whereupon flame atomic absorption spectrometry (FLAA) was used to analyze the remaining Cu^{2+} concentration in the supernatant. The removal percentage (%, R) and adsorption capacity (q_e, mg/g) of the adsorbent were, respectively, calculated using the following formulas:

$$\% R = {C_i - C_e}/_{C_0} \times 100\% \tag{3}$$

$$q_e = {V}/_M \times (C_i - C_e) \tag{4}$$

where C_i and C_e (mg/L) are the initial concentration and final concentration of the Cu^{2+} solution, respectively; V(L) is the volume of the Cu^{2+} solution; and M (g) is the quality of the penetrant.

Results and discussion

XRD crystal phase analysis

This study's objective was to convert calcium carbonate in the limestone sludge precursor material into eco-HAP. Figure 1a presents the XRD patterns of the eco-HAP synthesized at a hydrothermal temperature of 120 °C with various Ca/P molar ratios. The eco-HAP synthesized using a Ca/P molar ratio of 1 (LA3) was comparable to the standard chart JCPDS (09-0432) with the following diffraction peaks at 2θ: 25.90°, 31.74°, 32.54°, 40.19°, 45.30°, 49.46°, and 53.12°. This study posits that under high-temperature and high-pressure hydrothermal synthesis conditions, the Ca^{2+} first reacted with PO_4^{3-} to form β-TCP ($Ca_3(PO_4)_2$), which reacted with Ca^{2+} and OH^- to form eco-HAP crystals. Sample LA3 also presented a diffraction peak of beta tri-calcium phosphate (β-TCP) at 34.37°, a byproduct of eco-HAP synthesis. This study posits that this was due to a small quantity of Ca^{2+} in the mixed solution forming a precipitate of $Ca(OH)_2$ under high alkaline conditions (pH = 10), such that there was insufficient Ca^{2+} to react with all of the β-TCP [34].

Using the same hydrothermal temperature (120 °C) with a Ca/P molar ratio of 1.67, 2.33, or 3 (samples LA5, LA7, and LA9), this study observed 2θ diffraction peaks at 25.90° and 31.74°. This study posit that the high diffraction peak intensity of sample LA7 (Ca/P = 2.33) can be attributed to the availability of Ca^{2+} to react with PO_4^{3-} and OH^- to form eco-HAP [35]. Increasing the Ca/P molar ratio to 3.0 decreased the relative content of PO_4^{3-}, such that a portion of Ca^{2+} reacted with OH^- to form $Ca(OH)_2$, which was unsuitable for the formation of eco-HAP, resulting in a weaker diffraction peak.

Figure 1b presents the XRD patterns of eco-HAP at a hydrothermal temperature of 150 °C with various Ca/P molar ratios. Samples with a Ca/P molar ratio of 1 (LB3) presented 2θ diffraction peaks at 25.84°, 31.72°, 32.62°, 40.05°, 45.27°, 49.42°, and 53.21°. It appears that the first reaction involved the conversion of the aragonite phase (hexagonal) into calcite (hexagonal), which reacted with phosphate to form β-TCP (rhombohedral), eventually leading to the formation of a thermodynamically stable form of calcium phosphate (hexagonal) [36]. Sample LB3 also presented a diffraction peak at 34.37°, indicative of β-TCP. As with the eco-HAP synthesized at a hydrothermal temperature of 120 °C, increasing the molar ratio to 1.67, 2.33 or 3.0 produced diffraction peaks at 25.90° and 31.74°; however, the intensity of these peaks was higher, indicating higher crystallinity.

Figure 1c presents the XRD patterns of eco-HAP at a hydrothermal temperature of 180 °C with various Ca/P
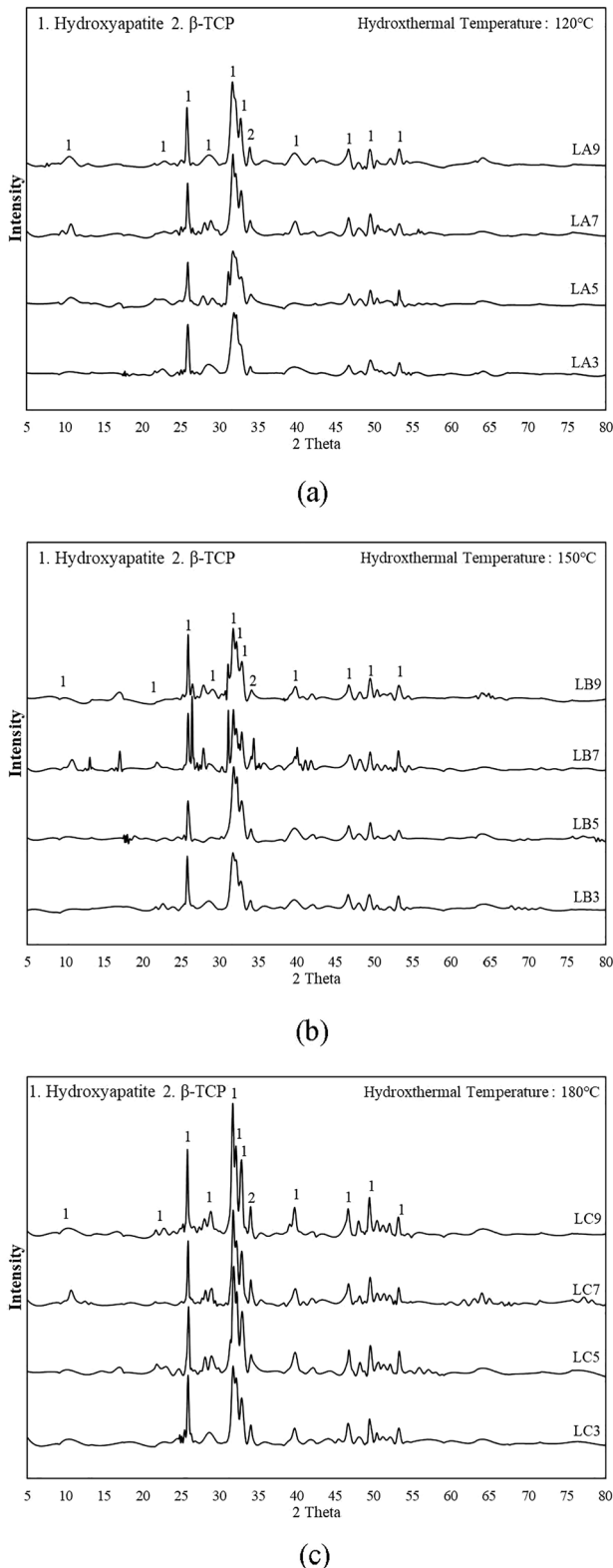
(a)

(b)

(c)

Fig. 1 XRD patterns of eco-HAP

Table 2 The crystallinity of eco-HAP

Sample	Crystallinity (%)	Crystallite size (nm)			
		002	211	310	Average
LA3	73.78	0.23	0.08	0.10	0.14
LA5	78.43	0.26	0.12	0.11	0.16
LA7	83.10	0.70	0.21	0.35	0.42
LA9	70.07	0.67	0.19	0.20	0.36
LB3	78.68	0.52	0.14	0.21	0.42
LB5	81.38	0.61	0.19	0.19	0.46
LB7	83.46	0.91	0.20	0.22	0.44
LB9	71.62	0.72	0.21	0.09	0.19
LC3	74.00	0.74	0.20	0.23	0.39
LC5	84.70	0.83	0.20	0.26	0.53
LC7	85.48	1.11	0.76	0.32	0.64
LC9	71.06	0.91	0.60	0.51	0.67

molar ratios. Samples with a Ca/P molar ratio of 1 (LC3) presented 2θ diffraction peaks at $2\theta = 25.81°$, $31.73°$, $32.58°$, $40.10°$, $45.24°$, $49.40°$, and $53.18°$. Strong peaks at $2\theta = 25.81°$, $31.7°$, and $32.58°$, respectively, corresponded to the (002), (211), and (300) planes of eco-HAP. The intensity ratio of the (002) to the (211) plane in their samples was far higher than that of the standard, indicating that the crystallization of eco-HAP occurred along the c-axis (Feng et al. 2016) [37]. Increasing the Ca/P molar ratio to 1.67, 2.33, and 3 (LC5, LC7 and LC9) led to an increase in the strength of the 2θ diffraction peaks at 25.90° and 31.74°. Increasing the hydrothermal temperature from 120 to 180 °C increased the intensity of the diffraction peaks at 25.81°, 31.73°, 32.58°, 40.10°, 45.24°, 49.40°, and 53.18°, which is indicative of higher crystallinity.

Table 2 lists the crystallinity of eco-HAP samples synthesized at various temperatures with various Ca/P molar ratios. In samples synthesized at 120 °C, the crystallinity varied as a function of Ca/P ratio, as follows: 1 (73.78%), 1.67 (78.43%), 2.33 (83.10%), and 3.0 (70.07%). The obvious drop in crystallinity under a Ca/P ratio of 3.0 can be attributed to a decrease in the quantity of PO_4^{3-}, such that a portion of Ca^{2+} reacted with OH^- to form $Ca(OH)_2$, which is ill-suited to the formation of eco-HAP crystals (Liu et al., 2018). Note that a high Ca/P ratio had the same effect, regardless of synthesis temperature. Increasing the hydrothermal synthesis temperature to 180 °C was shown to increase crystallinity, regardless of Ca/P ratio.

FE-SEM analysis

Figure 2a presents FE-SEM images of eco-HAP synthesized at a hydrothermal temperature of 120 °C with various Ca/P molar ratios. A Ca/P molar ratio of 1 resulted in eco-HAP particles with an elliptical shape. Increasing the Ca/P molar ratio to 1.67 resulted in slightly elongated particles. A Ca/P molar ratio of 2.33 or 3.0 resulted in particles with a pronounced rod shape, a length of 144–201 nm, and a width of 25–30 nm. Liu et al. (2018) [35] reported that under high-temperature and high-pressure conditions, the reaction of $Ca(OH)_2$ with PO_4^{3-} resulted in eco-HAP with high-intensity diffraction peaks. This study posits that increasing the Ca/P molar ratio increased the amount of $Ca(OH)_2$ available in the solution to react with PO_4^{3-}, resulting in the formation of rod-shaped eco-HAP. Note that these results are consistent with the XRD patterns.

Figure 2b presents FE-SEM images of eco-HAP synthesized at a hydrothermal temperature of 150 °C with various Ca/P molar ratios. A Ca/P molar ratio of 1 resulted in eco-HAP particles in the shape of short rods. Note that the length of the rods increased with the Ca/P ratio. Note also that the form of the eco-HAP crystals depended on the Ca/P molar ratio in the precursor solution as well as the

synthesis temperature and synthesis time. The eco-HAP crystals nucleated and grew from single sites to form rod-shaped particles. The agglomeration of adjacent crystals led to the formation of bundle-like structures, which formed in a stacked configuration.

Figure 2c presents FE-SEM images of eco-HAP synthesized at a hydrothermal temperature of 180 °C with various Ca/P molar ratios. A Ca/P molar ratio of 1 resulted in eco-HAP particles with a distinct rod shape, measuring 152.7 nm in length and 34.6 nm in width. Increasing the molar ratio to 3.0 increased the length of the particles to 241.9 nm and the width to 60.6 nm. Zhang et al. [38] reported that the Ca/P molar ratio had little effect on the length of crystals. Arfa et al. [39] reported that the Ca/P molar ratio was affected by the pH value but not the synthesis temperature. Taken together, these results indicate that synthesis temperature and Ca/P molar ratio affected the crystal size, crystallinity, and peak intensity of the eco-HAP.

Nitrogen adsorption and desorption curves

Figure 3a presents the N_2 adsorption/desorption isotherms of eco-HAP. The eco-HAP samples synthesized at 120 °C with a Ca/P molar ratio of 1 presented a type-IV
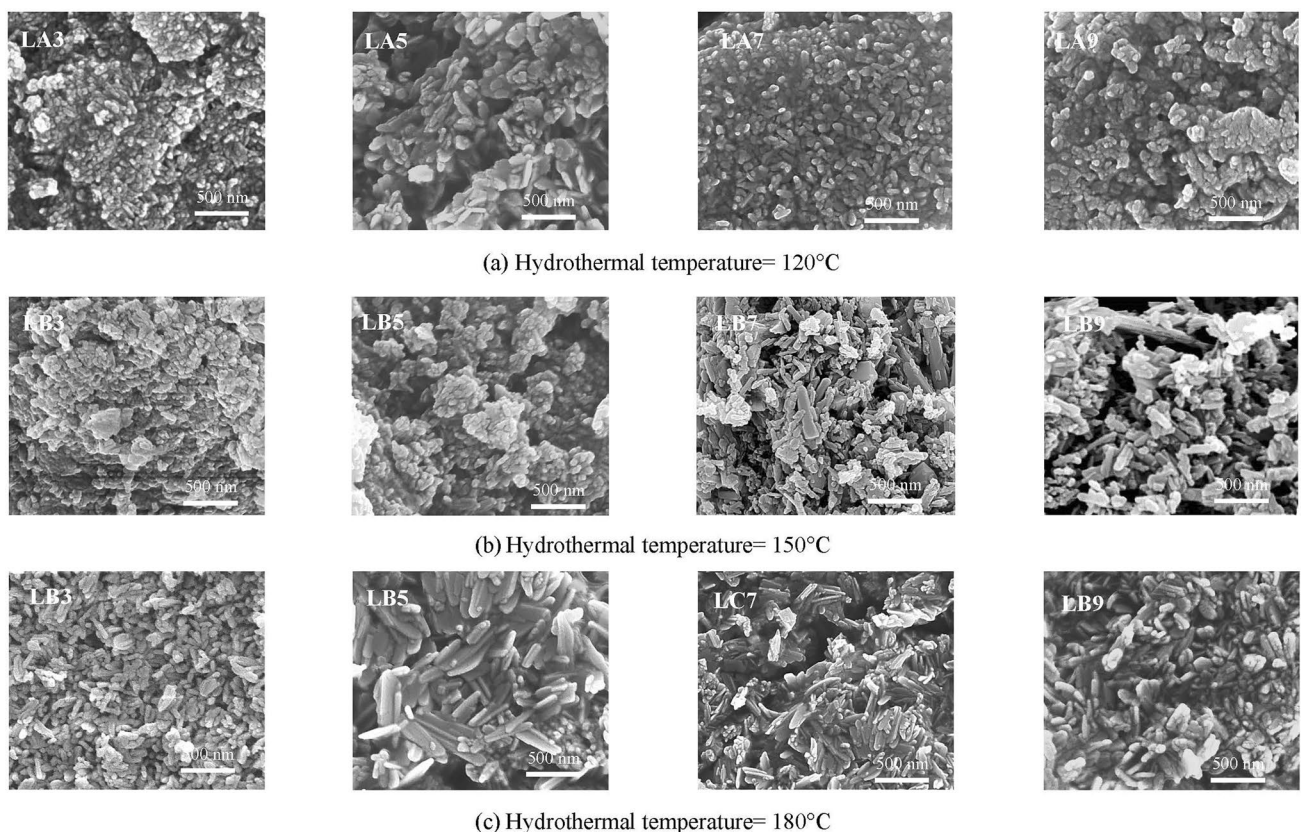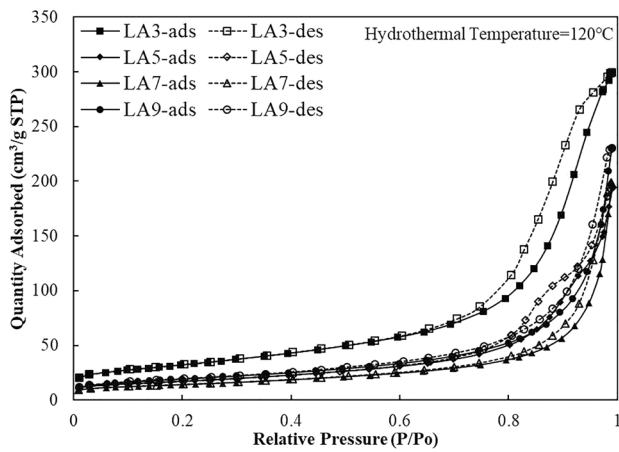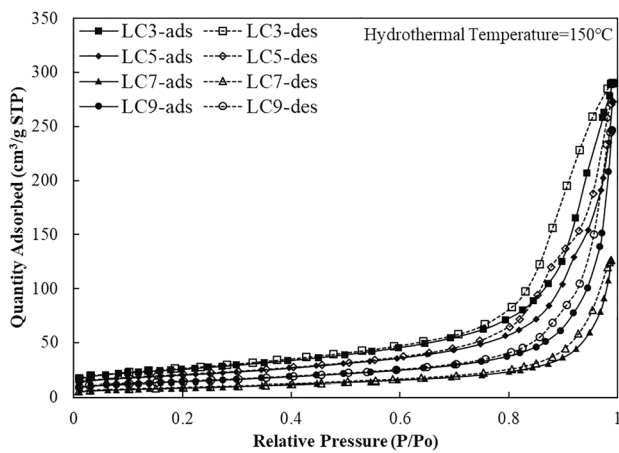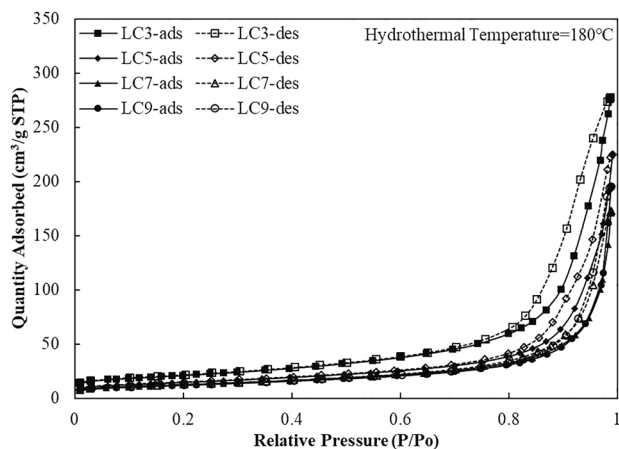

(a) Hydrothermal temperature= 120°C

(b) Hydrothermal temperature= 150°C

(c) Hydrothermal temperature= 180°C

Fig. 2 FE-SEM image of eco-HAP

(a) Hydrothermal Temperature=120°C

(b) Hydrothermal Temperature=150°C

(c) Hydrothermal Temperature=180°C

Fig. 3 Nitrogen adsorption isotherm and desorption curve of eco-HAP

adsorption isotherm curve (IUPAC classification), indicating a mesoporous structure and small nanoplate aggregates [40] and H3-type hysteresis loop. During adsorption, the number of N_2 molecules in the pores increased with the pressure, and the capillary condensation of N_2 molecules led to isotherm retention [41]. The maximum adsorption capacity LA3 was 299.42 cm^3/g STP with a specific surface area of 115.04 m^2/g. Eco-HAP samples synthesized at 120 °C with a Ca/P molar ratio of 2.33 presented a maximum adsorption capacity 199.02 cm^3/g STP and a specific surface area of 49.44 m^2/g. Wei et al. [42] reported that the crystallinity of eco-HAP is inversely proportional to the specific surface area of eco-HAP and the corresponding number of active sites.

Samples synthesized at 150 °C presented the same trend as those synthesized at 120 °C. The eco-HAP samples synthesized at 180 °C with a Ca/P molar ratio of 1 presented a specific surface area of 74.69 m^2/g and a maximum adsorption capacity of 277.21 cm^3/g STP, both of which are below those of samples synthesized at 120 °C.

Figure 4 presents the pore size distribution of eco-HAP. The eco-HAP samples synthesized at 120 °C with a Ca/P molar ratio of 1 presented a bimodal mesopore size distribution (3.21 nm and 14.44 nm). Increasing the Ca/P molar ratio to 2.33 resulted in a unimodal pore size distribution with significantly smaller pores (2.91 nm) [42]. The eco-HAP samples synthesized at 150 °C with a Ca/P molar ratio of 1 presented a bimodal mesopore size distribution (3.19 and 16.21 nm). Increasing the Ca/P molar ratio to 2.33 increased the pore size to 3.05 nm. The eco-HAP samples synthesized at 120 °C with a Ca/P molar ratio of 1 presented a bimodal mesopore size distribution (4.21 and 24.44 nm). Increasing the Ca/P molar ratio to 2.33 increased the pore size to 2.14 nm.
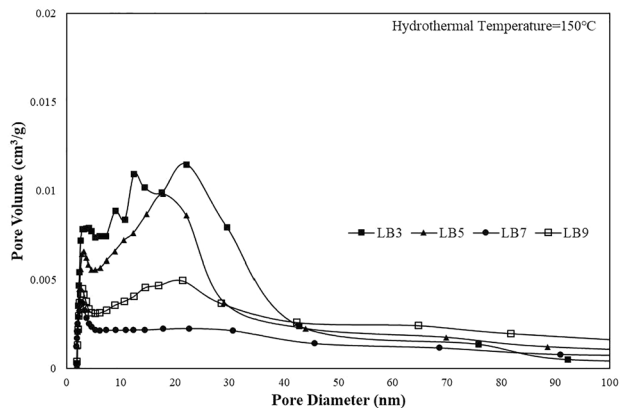
Adsorption kinetics of Cu^{2+} in eco-HAP

Figure 5a presents a graph showing the adsorption kinetics of Cu^{2+} in eco-HAP. The eco-HAP samples synthesized at 120 °C completed the reaction process within 20 min, wherein a rapid initial interaction between Cu^{2+} and eco-HAP gradually tapered off [8]. The adsorption capacity varied with the Ca/P molar ratio as follows: Ca/P = 1 (210 mg/g) and Ca/P = 2.33 (121.8 mg/g). Note that the adsorption capacity was inversely proportional to crystallinity.
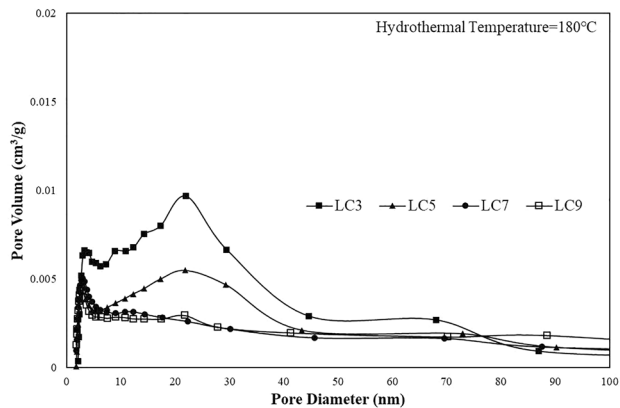
The eco-HAP samples synthesized at 150 °C completed the reaction process within 20 min. The adsorption capacity varied with the Ca/P molar ratio as follows: Ca/P = 1 (172.65 mg/g) and Ca/P = 2.33 (100 mg/g).
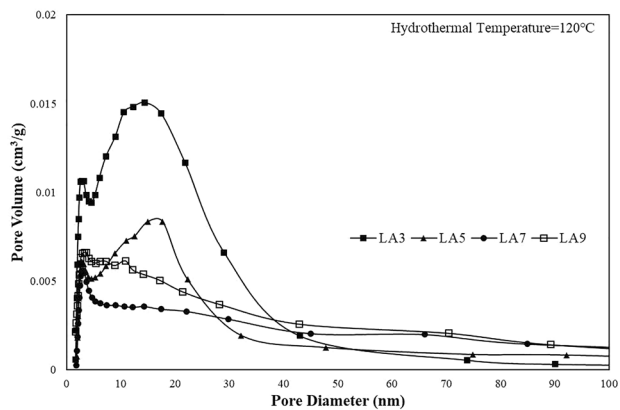
(a) Hydrothermal Temperature=120°C
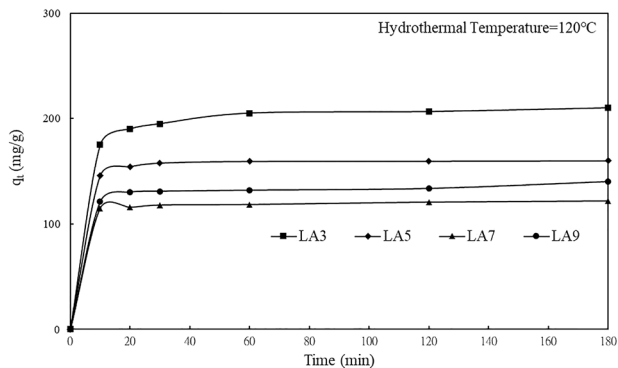

(b) Hydrothermal Temperature=150°C
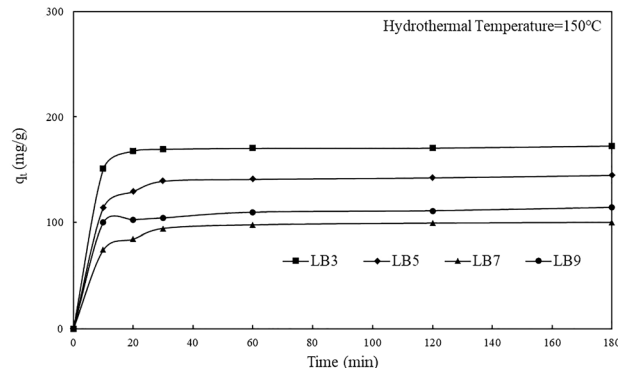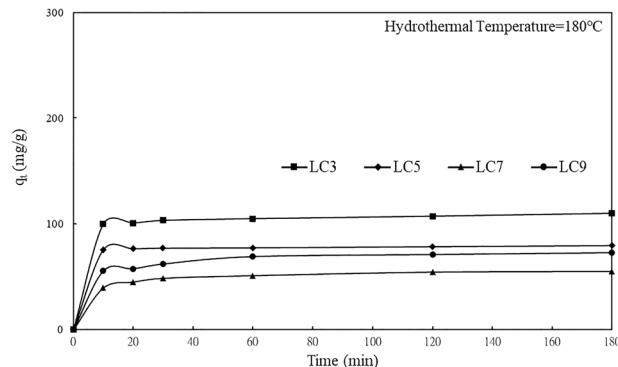

(c) Hydrothermal Temperature=180°C

Fig. 4 Pore size distribution of eco-HAP

(a) Hydrothermal Temperature=120°C

(b) Hydrothermal Temperature=150°C

(c) Hydrothermal Temperature=180°C

Fig. 5 Adsorption kinetics of Cu^{2+} in eco-HAP

The eco-HAP samples synthesized at 180 °C completed the reaction process within 20 min. The adsorption capacity varied with the Ca/P molar ratio as follows: Ca/P = 1 (110 mg/g) and Ca/P = 2.33 (55 mg/g). Again, adsorption capacity was inversely proportional to crystallinity.

The diffusion mechanism involved in the adsorption process was characterized using pseudo-first-order and pseudo-second-order kinetic models, based on the following formulas:

$$\ln\left(q_e - q_t\right) = \ln q_e - k_1 t \tag{5}$$

$$t/q_t = 1/k_2 q_e^2 + t/q_e \tag{6}$$

where q_e and q_t (mg/g), respectively, indicate the amount of Cu^{2+} adsorbed on the eco-HAP (mg/g) when the adsorption

Table 3 Adsorption kinetic parameters of Cu^{2+} on eco-HAP

Sample	Pseudo-first-order			Pseudo-second-order		
	q_e	k_1	R^2	q_e	k_2	R^2
LA3	28.45	0.0199	0.9349	476.19	1.00×10^{-3}	0.9999
LAS	4.70	0.0192	0.9618	416.67	9.60×10^{-3}	0.9999
LA7	6.67	0.0118	0.9287	312.50	2.38×10^{-3}	1.0000
LA9	17.55	0.0137	0.8446	357.14	1.91×10^{-3}	0.9999
LB3	8.21	0.019	0.9253	434.78	1.56×10^{-3}	0.9999
LB5	17.58	0.0197	0.9421	400.00	2.16×10^{-3}	0.9999
LB7	14.98	0.0226	0.9476	322.58	1.16×10^{-3}	0.9998
LB9	15.08	0.017	0.9822	333.33	1.45×10^{-3}	0.9998
LC3	11.15	0.0189	0.9822	400.00	4.70×10^{-4}	0.9991
LC5	3.49	0.0156	0.9490	312.50	1.38×10^{-3}	0.9997
LC7	12.50	0.0157	0.7793	270.27	1.40×10^{-3}	0.9997
LC9	17.15	0.0179	0.8936	277.78	1.12×10^{-3}	0.9990

reached equilibrium and time t (min); and k_1 and k_2 indicate the pseudo-first-order and pseudo-second-order rate constants (g/mg/min).

Table 3 lists the kinetic parameters of eco-HAP adsorbed lead ions based on the pseudo-first-order and pseudo-second-order kinetic models. Overall, the fitting effect of the pseudo-second-order kinetics model was better than that of the pseudo-first-order model, with an R^2 value of 0.9990–1.000. These results show that the eco-HAP controlled the exchange of ions and other chemical interactions between the adsorbent and adsorbate.

Removal efficiency of Cu^{2+} from aqueous solutions

Figure 6 presents a graph illustrating the influence of adsorbent quantity on the performance of the eco-HAP (LA3) in terms of Cu^{2+} removal (synthesis temperature = 120 °C and Ca/P molar ratio = 1). Increasing the quantity of adsorbent from 0.1 to 2 g/L increased the proportion of removed copper ions from 27 to 99.40%, due presumably to an increase in the number of adsorption sites. Overall, the removal performance of the eco-HAP increased with adsorbent quantity, regardless of the Ca/P molar ratio. Nonetheless, samples synthesized with a Ca/P molar ratio of 3.0 (2 g/L) removed only 79.75% of the dissolved copper ions, due presumably to higher crystallinity, which reduced the number of available adsorption sites as well as the dissolution of phosphate and hydroxyl radicals. The removal efficiency of samples synthesized at 120 °C (99.99%) exceeded that of samples synthesized at 180 °C (80.68%), presumably due to enhanced crystallinity.

Cu^{2+} adsorption isotherms of eco-HAP

Adsorption isotherms can be used to characterize the surface of adsorbents at the micro level as well as the adsorption capacity, adsorption strength, and absorption state. In this study employed the Langmuir and Freundlich equation as follows:

$$Q_e = H_h C_e \qquad (7)$$

$$1/q_e = 1/q_m K C_e + 1/q_e \qquad (8)$$

$$Ln q_e = ln K_f + n ln C_e \qquad (9)$$

Figure 7 presents the Langmuir models of eco-HAP synthesized at temperatures of 120, 150, and 180 °C as a function of Ca/P molar ratio. The R^2 values of eco-HAP in the adsorption of Cu^{2+} were as follows: 120 °C (0.96–0.98), 150 °C (0.97–0.99), and 180 °C (0.96–0.99). Overall, the Ca/P molar ratio was proportional to $R^2 = 1$.

Figure 8 presents the Freundlich models of eco-HAP. The R^2 values of eco-HAP in the adsorption of Cu^{2+} were as follows: 120 °C (0.94–0.98), 150 °C (0.93–0.96), and 180 °C (0.90–0.97). Overall, the Ca/P molar ratio was proportional to R^2, and the adsorption isotherm curves were more closely described using the Langmuir model.
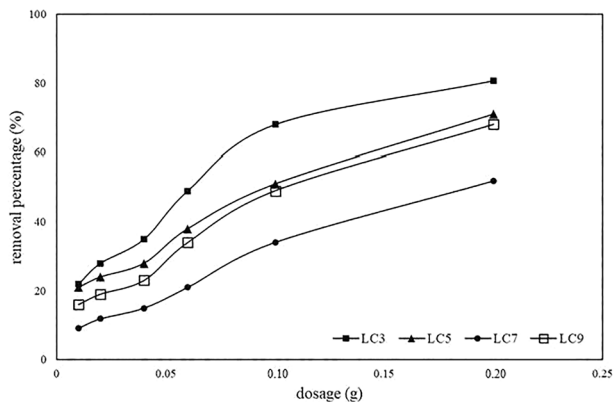
Adsorption mechanism

Varied parameters, initial adsorption concentration and adsorption time, are very vitalin evaluating the adsorption
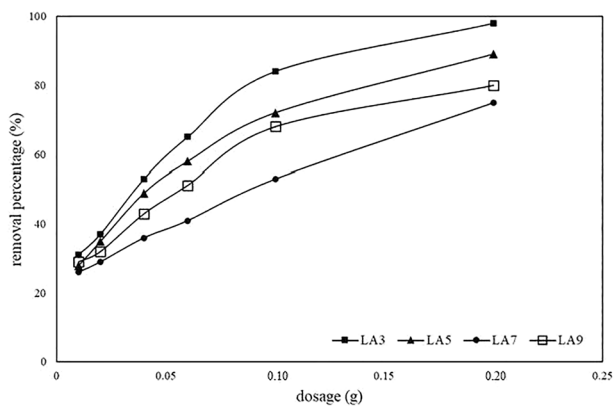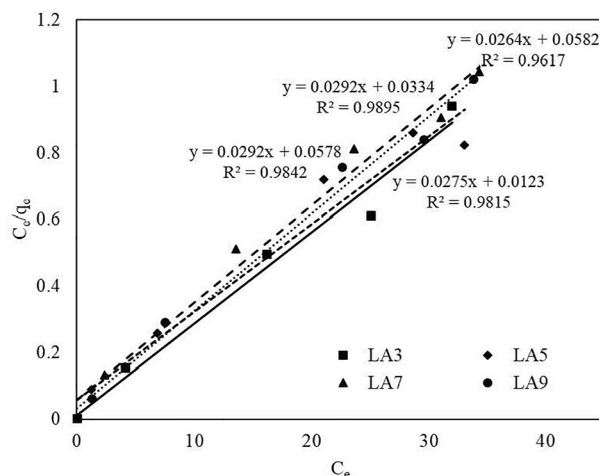
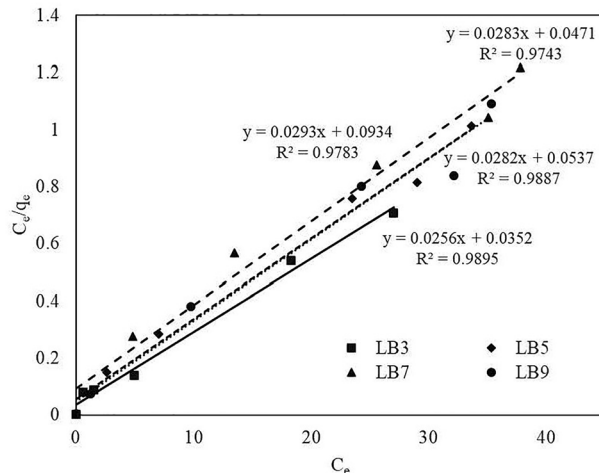(a) Hydrothermal Temperature=120°C
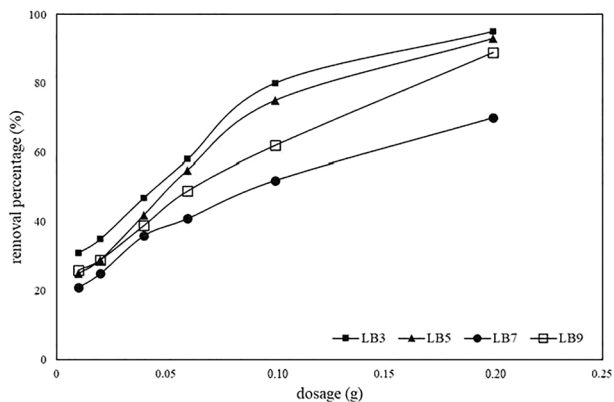
(b) Hydrothermal Temperature=150°C

(c) Hydrothermal Temperature=180°C

Fig. 6 The removal efficiency of eco-HAP removing Cu^{2+} from aqueous solutions
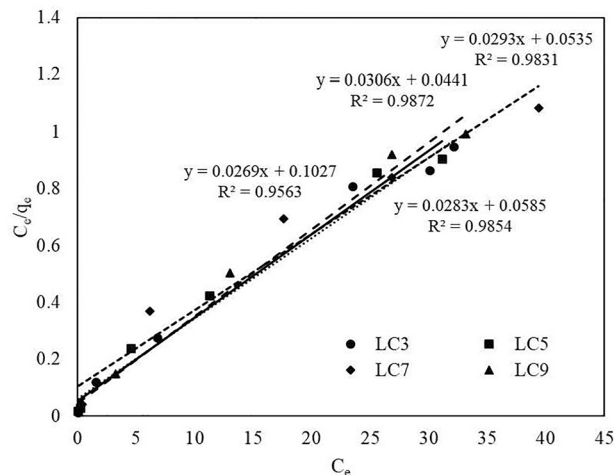

(a) Hydrothermal Temperature=120°C

(b) Hydrothermal Temperature=150°C

(c) Hydrothermal Temperature=180°C

Fig. 7 Langmuir diagram of Cu^{2+} adsorption by eco-HAP

capacity of heavy metal ions. As for the adsorption equilibrium isotherms and the adsorption kinetics, they are important measurements in diagnosing the adsorption mechanism and evaluating the adsorption efficiency. In this experiment, a series of batch equilibrium experiments were carried out to identify the effects of adsorption time (Fig. 5) and initial

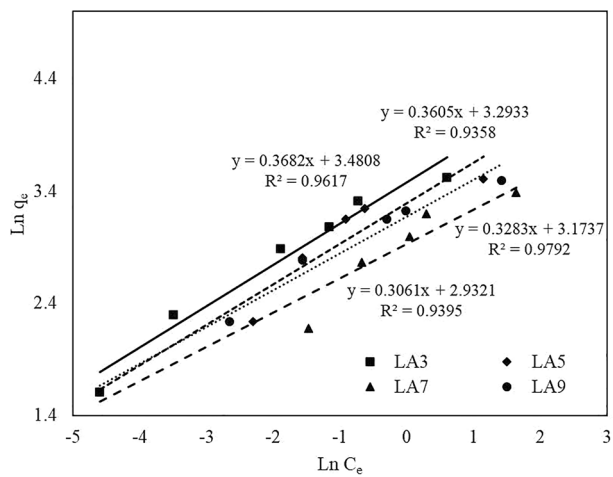(a) Hydrothermal Temperature=120°C
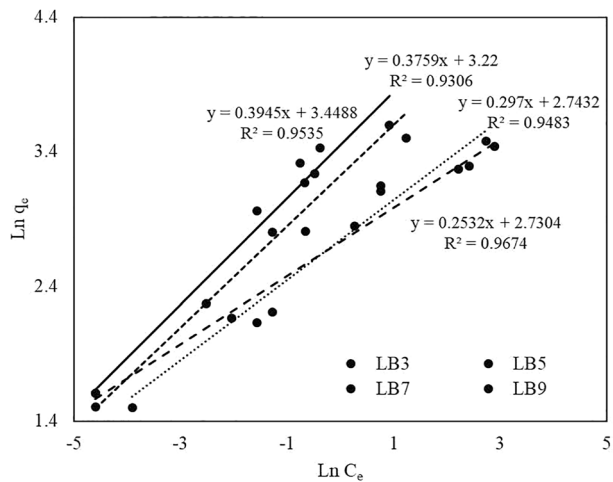

(b) Hydrothermal Temperature=150°C
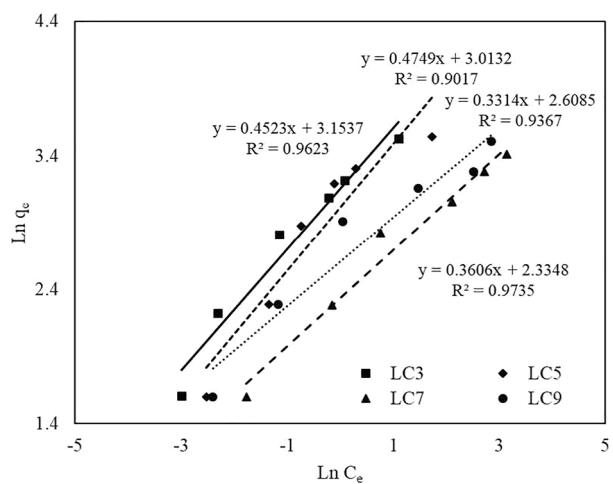

(c) Hydrothermal Temperature=180°C

Fig. 8 Freundlich diagram of Cu^{2+} adsorption by eco-HAP

adsorption concentration (Figs. 7 and 8) on the adsorption of Cu^{2+}. The mechanisms of eco-HAP removal Cu^{2+} in an aqueous solution are shown in Fig. 9. For the adsorption mechanism of Cu^{2+}, they were adsorbed on eco-HAP, which mainly relied on the ion exchange through substituting Ca^{2+} from the apatite lattice by a diffusion process according to Eq. (10):

$$\equiv Ca_{10}(PO_4)_6(OH)_2 + xCu^{2+} \rightarrow \equiv Ca_{10-x}Cu_xPO_4)_6(OH)_2 + xCu^{2+} \tag{10}$$
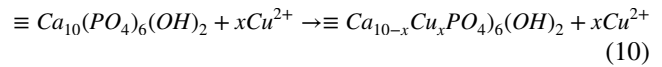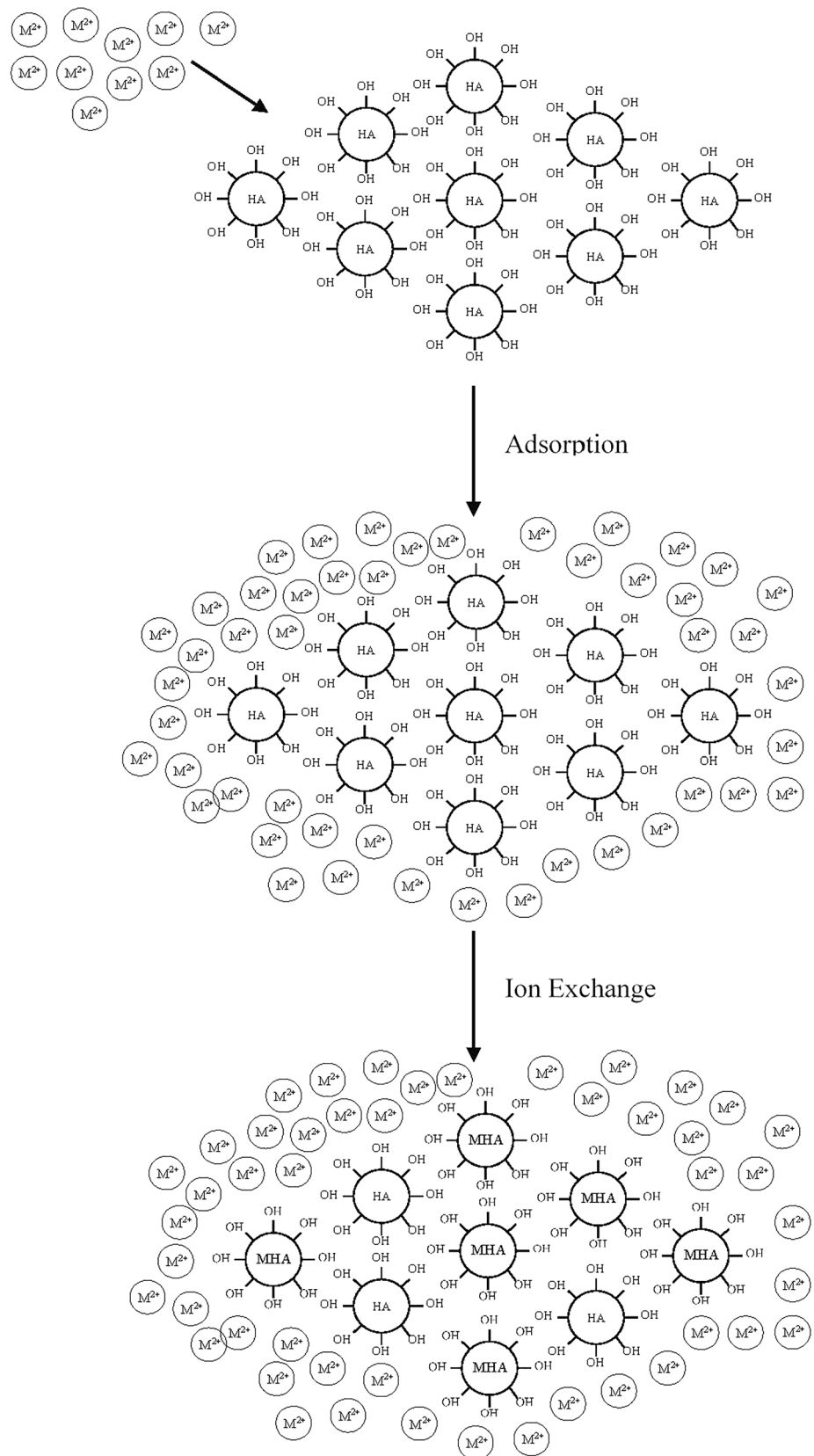
Conclusion

The limestone sludge is a promising alternative to expensive hydroxyapatite due to its low costs, satisfactory separation performance and sustainable feature. First, as a waste-to-resource strategy they are promising solutions to the waste disposal problems. Second, using wastes for limestone sludge reduces the raw material costs and the need for expensive and unrenewable raw materials (e.g. CaO). Third, synthetic HAp available on the market are very expensive due to the use of high-purity chemical reagents in the production of HAp. Finally, waste-derived hydroxyapatite could offer excellent pollutant removal performance due to its synergetic effect of adsorption properties. Therefore, more research efforts should be devoted to this exciting area to achieve long-term sustainability and move towards a circular economy.

This study developed a novel approach to the hydrothermal synthesis of eco-hydroxyapatite (eco-HPA) from recycled limestone sludge for the removal of Cu^{2+} from aqueous solutions. In the hydrothermal synthesis of eco-HAP under high-temperature and high-pressure conditions, Ca^{2+} first reacted with PO_4^{3-} to form β-TCP, which then reacted with Ca^{2+} and OH- to form eco-HAP crystals. Note that the sample synthesized at 120 °C with a Ca/P molar ratio of 1 presented a 2θ diffraction peak of β-TCP at 34.37°, a byproduct of eco-HAP synthesis. The as-prepared eco-HAP presented good adsorption capacity in the removal of Cu^{2+} from aqueous solutions. Under a hydrothermal temperature of 120 °C and Ca/P molar ratio of 1, it obtained hydroxyapatite (LA3) with an adsorption capacity of 210 mg/g. The adsorption kinetics closely fit the pseudo-second-order kinetic model ($R^2 = 0.9990$–1.000). The isotherms presented the strongest correlation with the Langmuir model ($R^2 = 0.97$–0.99). These results show that the eco-HAP controlled the exchange of ions and other chemical interactions between the adsorbent and adsorbate. The stability of the proposed material after adsorbing Cu^{2+} would also prevent secondary contamination.

Fig. 9 The mechanism of Cu^{2+} removal on eco-HAP

Declarations

Conflict of interest The authors declare they have no competing interests.

References

1. Amin MN, Khan K, Saleem MU, Khurram N, Niazi MUK (2017) Aging and curing temperature effects on compressive strength of mortar containing lime stone quarry dust and industrial granite sludge. Materials 10(6):642. https://doi.org/10.3390/ma10060642

2. Mageed AA, AbdelHaffez GS (2012) Utilization of limestone dust in brick making. JES J Eng Sci 40(3):913–922. https://doi.org/10.21608/jesaun.2012.114423

3. Felekoglu B (2007) Utilisation of high volumes of limestone quarry wastes in concrete industry (self-compacting concrete case). Resour Conserv Recycl 51(4):770–791. https://doi.org/10.1016/j.resconrec.2006.12.004

4. Maheswaran S, Ramesh Kumar V, Bhuvaneshwari B, Palani GS, Iyer NR (2011) Studies on lime sludge for partial replacement of cement. Appl Mech Mater 71:1015–1019. https://doi.org/10.4028/www.scientific.net/AMM.71-78.1015

5. Turgut P (2008) Properties of masonry blocks produced with waste limestone sawdust and glass powder. Constr Build Mater 22(7):1422–1427. https://doi.org/10.1016/j.conbuildmat.2007.04.008

6. Pellera FM, Giannis A, Kalderis D, Anastasiadou K, Stegmann R, Wang JY, Gidarakos E (2012) Adsorption of Cu (II) ions from aqueous solutions on biochars prepared from agricultural by-products. J Environ Manage 96(1):35–42. https://doi.org/10.1016/j.jenvman.2011.10.010

7. Semerciöz AS, Göğüş F, Celekli A, Bozkurt H (2017) Development of carbonaceous material from grapefruit peel with microwave implemented-low temperature hydrothermal carbonization technique for the adsorption of Cu (II). J Clean Prod 165:599–610. https://doi.org/10.1016/j.jclepro.2017.07.159

8. Jung KW, Lee SY, Choi JW, Lee YJ (2019) A facile one-pot hydrothermal synthesis of hydroxyapatite/biochar nanocomposites: adsorption behavior and mechanisms for the removal of copper (II) from aqueous media. Chem Eng J 369:529–541. https://doi.org/10.1016/j.cej.2019.03.102

9. Mushtaq M, Bhatti HN, Iqbal M, Noreen S (2019) Eriobotrya japonica seed biocomposite efficiency for copper adsorption: isotherms, kinetics, thermodynamic and desorption studies. J Environ Manage 176:21–33. https://doi.org/10.1016/j.jenvman.2016.03.013

10. Fu F, Wang Q (2011) Removal of heavy metal ions from wastewaters: a review. J Environ Manage 92(3):407–418. https://doi.org/10.1016/j.jenvman.2010.11.011

11. Wang YH, Lin SH, Juang RS (2003) Removal of heavy metal ions from aqueous solutions using various low-cost adsorbents. J Hazard Mater 102(2–3):291–302. https://doi.org/10.1016/S0304-3894(03)00218-8

12. O'Connell DW, Birkinshaw C, O'Dwyer TF (2008) Heavy metal adsorbents prepared from the modification of cellulose: a review. Bioresour Technol 99(15):6709–6724. https://doi.org/10.1016/j.biortech.2008.01.036

13. Kurniawan TA, Chan GY, Lo WH, Babel S (2006) Physico–chemical treatment techniques for wastewater laden with heavy metals. Chem Eng J 118(1–2):83–98. https://doi.org/10.1016/j.cej.2006.01.015

14. Galil N, Rebhun M (1990) Primary chemical treatment minimizing dependence on bioprocess in small treatment plants. Water Sci Technol 22(3–4):203–210. https://doi.org/10.2166/wst.1990.0202

15. Ye Y, Yang J, Jiang W, Kang J, Hu Y, Ngo HH, Liu Y (2018) Fluoride removal from water using a magnesia-pullulan composite in a continuous fixed-bed column. J Environ Manage 206:929–937. https://doi.org/10.1016/j.jenvman.2017.11.081

16. Yu S, Wang X, Liu Y, Chen Z, Wu Y, Liu Y, Pang H, Song G, Chen J, Wang X (2019) Efficient removal of uranium (VI) by layered double hydroxides supported nanoscale zero-valent iron: a combined experimental and spectroscopic studies. Chem Eng J 365:51–59. https://doi.org/10.1016/j.cej.2019.02.024

17. Apiratikul R, Pavasant P (2008) Sorption of Cu^{2+}, Cd^{2+}, and Pb^{2+} using modified zeolite from coal fly ash. Chem Eng J 144(2):245–258. https://doi.org/10.1016/j.cej.2008.01.038

18. Bhattacharyya KG, Gupta SS (2008) Influence of acid activation on adsorption of Ni (II) and Cu (II) on kaolinite and montmorillonite: kinetic and thermodynamic study. Chem Eng J 136(1):1–13. https://doi.org/10.1016/j.cej.2007.03.005

19. Al-Ghouti MA, Khraisheh MA, Tutuji M (2004) Flow injection potentiometric stripping analysis for study of adsorption of heavy metal ions onto modified diatomite. Chem Eng J 104(1–3):83–91. https://doi.org/10.1016/j.cej.2004.07.010

20. Šljivić M, Smičiklas I, Pejanović S, Plećaš I (2009) Comparative study of Cu^{2+} adsorption on a zeolite, a clay and a diatomite from Serbia. Appl Clay Sci 43(1):33–40. https://doi.org/10.1016/j.clay.2008.07.009

21. Feng Y, Gong JL, Zeng GM, Niu QY, Zhang HY, Niu CG, Deng JH, Yan M (2010) Adsorption of Cd (II) and Zn (II) from aqueous solutions using magnetic hydroxyapatite nanoparticles as adsorbents. Chem Eng J 162(2):487–494. https://doi.org/10.1016/j.cej.2010.05.049

22. Lusvardi G, Malavasi G, Menabue L, Saladini M (2002) Removal of cadmium ion by means of synthetic hydroxyapatite. Waste Manage 22(8):853–857. https://doi.org/10.1016/S0956-053X(02)00078-8

23. Chaturvedi PK, Seth CS, Misra V (2006) Sorption kinetics and leachability of heavy metal from the contaminated soil amended with immobilizing agent (humus soil and hydroxyapatite). Chemosphere 64(7):1109–1114. https://doi.org/10.1016/j.chemosphere.2005.11.077

24. Hernández-Cocoletzi H, Salinas RA, Águila-Almanza E, Rubio-Rosas E, Chai WS, Chew KW, Mariscal-Hernández C, Show PL (2020) Natural hydroxyapatite from fishbone waste for the rapid adsorption of heavy metals of aqueous effluent. Environ Technol Innov 20:101109. https://doi.org/10.1016/j.eti.2020.101109

25. Smičiklas I, Dimović S, Plećaš I, Mitrić M (2006) Removal of Co^{2+} from aqueous solutions by hydroxyapatite. Water Res 40(12):2267–2274. https://doi.org/10.1016/j.watres.2006.04.031

26. Sheha RR (2007) Sorption behavior of Zn (II) ions on synthesized hydroxyapatites. J Colloid Interface Sci 310(1):18–26. https://doi.org/10.1016/j.jcis.2007.01.047

27. Corami A, Mignardi S, Ferrini V (2007) Copper and zinc decontamination from single-and binary-metal solutions using hydroxyapatite. J Hazard Mater 146(1–2):164–170. https://doi.org/10.1016/j.jhazmat.2006.12.003

28. Ayodele O, Olusegun SJ, Oluwasina OO, Okoronkwo EA, Olanipekun EO, Mohallem ND, Guimarães WG, de M Gomes BLF, de O Souza G, Duarte HA (2021) Experimental and theoretical studies of the adsorption of Cu and Ni ions from wastewater by hydroxyapatite derived from eggshells. Environ. Nanotechnol Monit Manag 15:100439. https://doi.org/10.1016/j.enmm.2021.100439

29. Wang YY, Liu YX, Lu HH, Yang RQ, Yang SM (2018) Competitive adsorption of Pb (II), Cu (II), and Zn (II) ions onto hydroxyapatite-biochar nanocomposite in aqueous solutions. J Solid State Chem 261:53–61. https://doi.org/10.1016/j.jssc.2018.02.010

30. Wang H, Yan K, Xing H, Chen J, Lu R (2021) Effective removal of Cu^{2+} from aqueous solution by synthetic abalone shell hydroxyapatite microspheres adsorbent. Environ Technol Innov 23:101663. https://doi.org/10.1016/j.eti.2021.101663

31. Chen Y, Li M, Li Y, Liu Y, Chen Y, Li H, Li L, Xu F, Jiang H, Chen L (2021) Hydroxyapatite modified sludge-based biochar for the adsorption of Cu^{2+} and Cd^{2+}: adsorption behavior and mechanisms. Bioresour Technol 321:124413. https://doi.org/10.1016/j.biortech.2020.124413

32. Iqbal A, Sattar H, Haider R, Munir S (2019) Synthesis and characterization of pure phase zeolite 4A from coal fly ash. J Clean Prod 219:258–267. https://doi.org/10.1016/j.jclepro.2019.02.066

33. Farzadi A, Bakhshi F, Hashjin MS, Eydivand MA, Osman NA (2014) Magnesium incorporated hydroxyapatite: synthesis and structural properties characterization. Ceram Int 40(4):6021–6029. https://doi.org/10.1016/j.ceramint.2013.11.051

34. Zhang X, Vecchio KS (2007) Hydrothermal synthesis of hydroxyapatite rods. J Cryst Growth 308(1):133–140. https://doi.org/10.1016/j.jcrysgro.2007.07.059

35. Liu W, Qiana G, Liu L, Zhang B, Fan X (2018) A simple method to controlled synthesis of nano hydroxyapatite in different particle size. Mater Lett 217(15):177–180. https://doi.org/10.1016/j.matlet.2018.01.079

36. Mohan N, Palangadan R, Fernandez FB, Varma H (2018) Preparation of hydroxyapatite porous scaffold from a 'coral-like' synthetic inorganic precursor for use as a bone substitute and a drug delivery vehicle. Mater Sci Eng C 92:329–337. https://doi.org/10.1016/j.msec.2018.06.064

37. Feng G, Cheng X, Xie D, Wang K, Zhang B (2016) Fabrication and characterization of nano prism-like hydroxyapatite coating on porous titanium substrate by combined biomimetic-hydrothermal method. Mater Lett 163:134–137. https://doi.org/10.1016/j.matlet.2015.10.063

38. Zhang G, Chen J, Yang S, Yu Q, Wang Z, Zhang Q (2011) Preparation of amino-acid-regulated hydroxyapatite particles by hydrothermal method. Mater Lett 65:572–574. https://doi.org/10.1016/j.matlet.2010.10.078

39. Arfa BAEB, Salvado IMM, Frade JR, Pullar RC (2016) Fast route for synthesis of stoichiometric hydroxyapatite by employing the Taguchi method. Mater Des 109:547–555. https://doi.org/10.1016/2Fj.matdes.2016.07.083

40. Xia X, Shen J, Cao F, Wang C, Tang M, Zhang Q, Wei S (2019) A facile synthesis of hydroxyapatite for effective removal strontium ion. J Hazard Mater 368:326–335. https://doi.org/10.1016/j.jhazmat.2019.01.040

41. Sabu U, Logesh G, Rashad M, Joy A, Balasubramanian M (2019) Microwave assisted synthesis of biomorphic hydroxyapatite. Ceram Int 45(6):6718–6722. https://doi.org/10.1016/j.ceramint.2018.12.161

42. Wei W, Sun R, Jin Z, Cui J, Wei Z (2014) Hydroxyapatite–gelatin nanocomposite as a novel adsorbent for nitrobenzene removal from aqueous solution. Appl Surf Sci 292:1020–1029. https://doi.org/10.1016/j.apsusc.2013.12.127